A Hierarchical LiDAR Simulation Framework Incorporating Physical Attenuation Response in Autonomous Driving Scenarios

Tengchao Huang, *Student Member, IEEE*, Shuang Song, *Student Member, IEEE*, Huosheng Hu, *Life Senior Member, IEEE*, Yunlong Gao, Guifang Shao, and Qingyuan Zhu, *Senior Member, IEEE*

***Abstract*— This paper presents a hierarchical LiDAR simulation framework to address the challenges of accurately simulating LiDAR data in autonomous driving scenarios. The framework utilizes a homology mapping approach to integrate LiDAR responses hierarchically at three levels: the instantaneous power response, environmental optical channel response, and target reflection response of LiDAR. This allows for the dynamic coupling of LiDAR geometric and physical models with varying environmental parameters. By integrating an array of interactions intrinsic to the LiDAR system and its external environment, the proposed model can provide high-fidelity LiDAR point cloud simulations. The effectiveness of the simulated point clouds has been validated through extensive experiments using actual LiDAR data and detection algorithms trained on existing datasets. The experimental results show that the proposed method has the potential to improve the realism of LiDAR simulations and the accumulation of challenging perception data.**

***Index Terms*— LiDAR, physical attenuation response, simulated point cloud, simulation test, autonomous vehicles.**

I. Introduction

THE effective implementation of autonomous driving technology requires a significant amount of data collection to enhance the performance and robustness of perception algorithms [1], [2], [3]. However, data acquisition through real-world driving is constrained by public safety concerns, which limits the ability to test challenging driving scenarios over extended periods [4], [5]. In contrast, computer-based simulations of autonomous driving offer a safer and more efficient alternative [6]. By orchestrating various driving situations in controlled virtual environments and emulating sensor data capture, these simulations can bridge the gap in obtaining nuanced perception data that real-world drives might not always afford [7]. Consequently, vehicle sensor simulation has become an essential component of the test and validation processes for autonomous vehicle perception algorithms.

LiDAR is one of the essential components of vehicular perception systems [8]. With the superior 3D panoramic scanning capabilities, LiDAR provides vehicles with an omnidirectional perspective to perceive environmental dynamics [9]. The construction of its high-fidelity models in virtual environments has the potential to broaden avenues for data acquisition in vehicular perception [10]. Currently, advanced autonomous driving simulators, such as Carla [11] and AirSim [12], can formulate simplified LiDAR models based on the geometric relationship between sensors and their environment, subsequently producing 3D point clouds. Empirical endeavors validate that these simulators can markedly enhance the accumulation of point cloud data across diverse traffic scenarios [13]. However, in pursuit of computational efficiency, these simulation approaches often overlook the inherent physical responses of LiDAR laser signals under real-world conditions. Such neglect can result in point cloud data that is far from reality.

In real traffic environments, the power of active pulse laser signals is prone to attenuate in aerosol-rich environments (e.g., rain, fog, and haze) and on surfaces that exhibit incomplete reflection [14]. The attenuation of signal power can lead to inconsistencies in the measurement distances across different laser beams, consequently giving rise to point clouds with diverse density distributions [15]. To elucidate this physical attenuation, various modeling techniques have been devised to capture the diverse response processes of LiDAR [16], [17]. For instance, within the domain of sensor design, researchers have formulated a power model for both emission and reception of signals, based on the inherent power consumption of LiDAR systems [18]. Similarly, in the arenas of environmental monitoring and laser imaging, physical models have been built to address laser scattering and reflection mechanisms [19]. While these models accurately describe the physical attenuation effects of LiDAR within their individual applications, their focused scopes render the interrelations among them remain divided.

Within the sphere of autonomous driving, a comprehensive measurement cycle of LiDAR typically spans a gamut of

Manuscript received 13 July 2023; revised 31 October 2023; accepted 27 November 2023. This work was supported in part by the National Key Research and Development Program of China under Grant 2022YFB3206605, in part by the National Natural Science Foundation of China under Grant 52075461, and in part by the Fujian Province University Industry-Academic Cooperation Project of China under Grant 2021H6019. The Associate Editor for this article was Y. Wiseman. *(Corresponding author: Qingyuan Zhu.)*

Tengchao Huang, Shuang Song, Yunlong Gao, Guifang Shao, and Qingyuan Zhu are with the Pen-Tung Sah Institute of Micro-Nano Science and Technology, Xiamen University, Xiamen 361000, China (e-mail: huangtengchao@stu.xmu.edu.cn; songs@stu.xmu.edu.cn; gaoyl@xmu.edu.cn; gfshao@xmu.edu.cn; zhuqy@xmu.edu.cn).

Huosheng Hu is with the School of Computer and Electronics Engineering, University of Essex, CO4 3SQ Colchester, U.K. (e-mail: hhu@essex.ac.uk).

This article has supplementary downloadable material available at https://doi.org/10.1109/TITS.2023.3340676, provided by the authors.

both physical and geometric mechanisms, encompassing laser signal power responses, dynamic environmental interactions, and point cloud imaging paradigms. To achieve a high-fidelity LiDAR representation, it becomes imperative to engage in multi-model coupling. However, the inherent diversities within these physical models can render the interrelations of their intrinsic parameters less discernible. Furthermore, the absence of an intuitive relationship between LiDAR's physical and geometric representations can lead to ambiguities and inconsistencies in model mapping, potentially complicating the integration of multiple models.

To address this challenge, we propose a hierarchical LiDAR simulation framework, tailored specifically for autonomous driving applications. Specifically, at the physical level, to ensure cohesive interplay among diverse physical parameters, we have architected a comprehensive signal transmission model that seamlessly links the instantaneous power response, the environmental optical channel response, and the target reflection response of the laser signals. Concurrently, at the geometric imaging level, we employ a homology mapping approach, hierarchically integrating these physical responses throughout the LiDAR's geometric measurement process, achieving synchronous amalgamation of both physical and geometric responses.

The proposed LiDAR simulation framework generates point cloud distributions that can reflect dynamic physical environment changes, thereby enhancing the realism of the point cloud data. The specific contributions of our work are outlined as follows:

- To tackle the challenges of integrating multiple LiDAR responses, we propose a hierarchical framework to systematically categorize the LiDAR responses across physical, geometric, and environmental levels.
- Addressing the parameter associations across various physical models, we establish a unified physical model to integrate instantaneous power response, optical channel response and target reflection response of LiDAR, holistically representing the physical attributes of lasers.
- Addressing inter-model coupling, we propose a homology mapping approach that streamlines the association from LiDAR physical parameters to geometric variables, ensuring efficient linkage of models across layers.
- Extensive experiments on actual LiDAR sensor tests and mainstream detection algorithms have confirmed the effectiveness of the simulated point clouds.

The rest of the paper is structured as follows. Section II reviews related work in LiDAR simulation. Section III details the physical modeling and integration methods of the proposed LiDAR hierarchical framework. Section IV presents the implementation and deployment of the method. Section V offers a comprehensive analysis of the applicability and effectiveness of the proposed model. Finally, a brief conclusion and future work are described in Section VI.

II. Related Work

A. LiDAR Models for Autonomous Driving Simulator

The LiDAR geometric model is a common paradigm utilized during measurements to deduce the distances between LiDAR sensors and their environment. Modern autonomous driving simulators employ this model to simulate LiDAR behavior. Specifically, AirSim deploys a geometry-based mapping technique, extracting surface nodes of virtual objects into point clouds through computer rendering [20]. However, this purely geometric method often oversimplifies the dynamic variations within point clouds. In contrast, Carla enriches this model by leveraging ray-casting techniques rooted in virtual physics-based engines. By computing intersections of rays originating from sensor points with virtual objects, Carla efficiently generates dynamic point clouds for traffic scenarios [21]. Similarly, LGSVL introduces a more open approach, boasting enhanced flexibility through customizable LiDAR configurations, encompassing field of view, rotation, channels, and Signal-to-Noise Rate (SNR) [22].

Such simulators benefit from the computational efficiency of geometric models, enabling rapid generation of extensive point cloud data. However, they overlook the complex physical attributes of LiDAR signals, which is a significant shortcoming. Heinzler et al. found that under varying environmental conditions, lasers experience different levels of signal intensity attenuation, potentially leading to unevenly sparse point cloud data across diverse object surfaces [23]. Consequently, the idealized point clouds generated by geometric models may introduce potential inaccuracies during real-world perception algorithm test.

B. Applications Status of LiDAR Physical Models

Compared to geometric models, the LiDAR physical model offers an expanded description of the physical interactions of lasers. Several mature modeling methods have been developed to address specific application scenarios.

In sensor design, power models for laser signals, driven by internal power consumption, are pivotal in guiding sensors and optimizing signal responses. Rasshofer et al. improved an energy transfer model, delving into the power spectrum functions intrinsic to LiDAR signal transmission and reception, capturing the subtleties of laser signal feedback [24]. Wisemen elucidated the measurement mechanism of pulsed waves, introducing an ultrasonic-assisted system to expand vehicle perception coverage [25]. Chen et al. enhanced the robustness of LiDAR against interference by instituting a programmable minimum interval time for laser pulses at specified power thresholds [26]. These investigations have advanced the development of laser signal models, elucidating the complexities within the LiDAR measurement mechanism. Nonetheless, current simulations have yet to identify effective technical solutions that bridge the LiDAR geometric model with the inherent physical parameters of the power model, all the while preserving model simplicity.

In environmental monitoring, researchers primarily investigate the optical channel attenuation of laser rays to decipher environmental parameters, resulting in numerous empirical formulas characterizing the optical channel responses of laser signals. Geiger et al. developed a compensation algorithm to correct laser attenuation curves, drawing on experimental result of laser scattering in fog [27]. Zhao et al. statistically analyzed rainwater's size and distribution in rainy

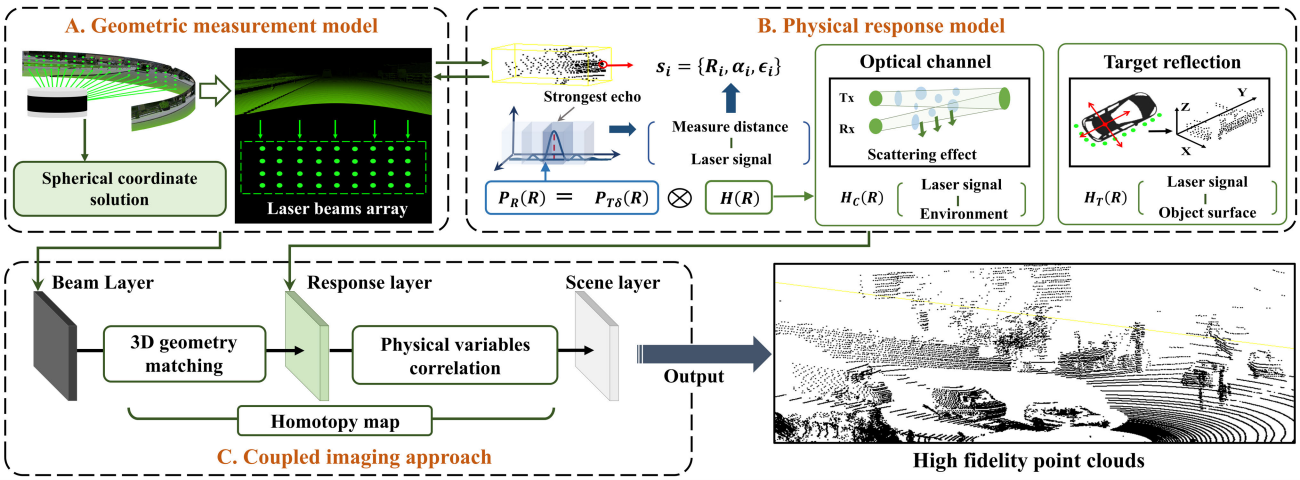

Fig. 1. Overall schematic diagram of hierarchical LiDAR simulation framework.

scenes, subsequently establishing a laser attenuation model that incorporated aerosol extinction coefficients [28]. Kutila et al. considered the interference from rain and fog on laser signal echoes, formulating a backward scattering model to delineate laser noise distribution in aerosol environments [29]. These methods can effectively analyze laser response changes under static environmental parameters. Yet, real-world driving conditions are inherently variable. Employing dynamic solutions for these empirical formulas might compromise the model's unique solution properties

In laser imaging, researchers emphasize the reflection effect of lasers on object surfaces, attributing point cloud imaging distributions to surface optical properties and laser angles. Yang et al. derived a formula for the relationship between reflection intensity and material properties by analyzing the point cloud imaging quality of measured traffic participants [30]. Molina et al. simulated the LiDAR imaging process using a graphical approach and generated point cloud data based on the LiDAR's forward field of view angle [31]. Grollius et al. designed a target simulator based on the time difference of the reflection, utilizing the principle of LiDAR's reflective perception imaging [32]. These methodologies could significantly enhance the availability of physical models for point cloud imaging. However, in traffic scenarios characterized by large-scale interactions, the sequential analysis of imaging patterns from individual LiDAR beams imposes a substantial computational burden.

In summary, the emphasis of LiDAR's geometric and physical modeling methods diverges considerably across different application domains. As a result, the absence of cohesive linkage between physical parameters of varied processes may lead to model redundancy and increase complexity in autonomous driving simulations. Moreover, since LiDAR perception is a dynamic process, when the physical models are coupled with the existing geometric models, the static solving paradigm of the physical models might restrict the order of parameter derivation in the integrated model, subsequently impacting the dynamic generation of point clouds. In this paper, we propose a hierarchical LiDAR simulation framework to address these challenges, which stratifies the physical and geometric models and introduces a homology mapping approach to correlate their respective parameters and variables. Notably, this framework doesn't deviate from the foundational solution of numerous simulation approaches, but rather augments the LiDAR geometric model with a physical layering.

III. LiDAR Sensor Simulation Method

This work is focused on three core components: geometric measurements, physical responses, and coupled imaging. As depicted in Fig. 1, a hierarchical framework systematically integrates multiple LiDAR responses. Firstly, within the section of geometric measurement model, a solution based on spherical coordinates is utilized to construct a structured laser beam array, aiming for the emulation of LiDAR's 3D scanning mode. Secondly, considering actual physical responses, the instantaneous power response model of the LiDAR system is integrated with attenuation models of laser signals across environmental optical channels and target reflections. This integration aims to build a cohesive association among diverse physical parameters. Finally, in the coupled imaging phase, the physical variables of the LiDAR system are cohesively linked with the geometric laser beam array. This establishes a homology mapping relationship, ensuring the alignment of point cloud data derivation with the perpetually shifting environment.

A. Geometric Measurement Model

The geometric measurement model serves as the foundation for calculating the position and orientation of objects in LiDAR measurements. Typically, the maximum measurement range of vehicular LiDAR does not exceed 200 meters, with a data acquisition frequency of approximately 20Hz. The laser measurement, based on the speed of light propagation, usually falls within the 100-200ns range [33]. Therefore, the laser response of the measurement model can be considered an instantaneous response, provided it remains within the sampling frequency limit.

Within the 3D scanning modes, the position and orientation of a target object in relation to the LiDAR sensor can be depicted by the relative positioning and direction of the laser collision points. As shown in Fig. 2, a geometric measurement

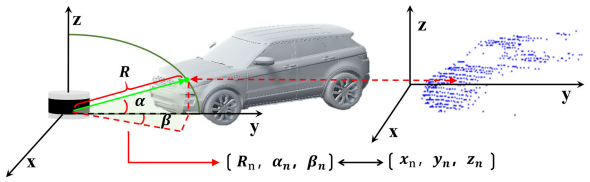

Fig. 2. Schematic diagram of LiDAR geometric measurement.

model rooted in the spherical coordinate system, with the sensor's center as the origin, has been constructed. By utilizing the collision information of virtual rays, a 3D coordinate sequence is outputted, denoted as

$$C_{(s_i)} = \{R_i, \alpha_i, \beta_i\}, \ and \ i \in N^+. \tag{1}$$

To apply the point cloud generated by the LiDAR measurement model to autonomous driving algorithms, we adopt the data encoding method employed for actual LiDAR point clouds. Specifically, the data is stored using a Cartesian coordinate system, with the coordinate origin at the sensor's center. Based on the conversion relationship between spherical and Cartesian coordinates, $C_{(s_i)}$ can be transformed into $C_{(p_i)}$ using equation (2). The encoding order starts from the x-axis, with measurements taken counterclockwise, and then written layer by layer from top to bottom along the z-axis.

$$C_{(p_i)} = \begin{bmatrix} x_i \\ y_i \\ z_i \end{bmatrix} = \begin{bmatrix} R_i \cos(\alpha_i)\cos(\beta_i) \\ R_i \sin(\alpha_i)\cos(\beta_i) \\ R_i \sin(\beta_i) \end{bmatrix}, \ and \ i \in N^+ \tag{2}$$

However, compared to Cartesian coordinates, we believe that the spherical coordinate system model, which better reflects the LiDAR measurement principle, is more conducive to integration with the physical model. Therefore, our subsequent signal attenuation model is primarily based on the spherical coordinate model. It should note that the point cloud data is converted into the standardized point cloud packet format in the Cartesian coordinate system only when it is applied in algorithm testing.

B. Signal Physical Response Model

In modeling LiDAR physical systems, it is imperative to accurately capture the attenuation of the laser signal throughout the entire measurement cycle. According to the transmission interplay of the laser signal among the sensor, environment, and target, we establish a multi-physical model that is shown in Fig. 3. More specifically, it encompasses three components as follows:

a) Instantaneous power response: we formulated a power model that correlates the emitted laser pulse P_T with the strongest echo P_R, based on system parameter at the sensor's transmission and reception. Using this as a foundation, we incorporated both the optical channel response at the transmission end and the reflection response at the target end, guided by the spatial pulse function $H(R)$.

b) Optical channel response: We established a relational model between optical channel response $H_C(R)$ and energy attenuation rate $T(R)$ by coordinating the connection among signal power, extinction coefficient, and environmental visibility, aiming to derive the optical channel power attenuation for various visibility scenarios.

c) Target reflection response: we integrated the object's surface diffuse reflection coefficient and modeled the power interplay for different lasers in terms of their optical incidence and reflection characteristics.

The three response mechanisms are sequentially linked by the signal's power transmission attenuation, effectively correlating the LiDAR system parameters, environmental visibility metrics, and target reflectivity.

1) Instantaneous Power Response: The power model of laser signal principally characterizes the internal energy consumption of the LiDAR system. Focusing on the pulse-type LiDAR, the emitted signal power P_T of a single laser beam can be defined using the sine-squared function.

$$P_T(t) = \begin{cases} P_0 \sin^2(\dfrac{\pi}{2\tau_H} t) & 0 \le t \le 2\tau_H; \\ 0 & else. \end{cases} \tag{3}$$

where P_0 is the peak voltage of the LiDAR's emitted pulse, τ_H is the half-power pulse width.

In LiDAR systems, peak power P_0 values typically reach 80W, corresponding to a pulse energy of approximately 1.6μJ. Notably, this emitted laser power often dictates the maximum detectable range of the sensor in practical applications. Building on this and considering the non-elastic scattering interactions of the laser with ambient aerosol particles, Hahner et al. [34] proposed that the received signal power can be calculated as the convolution between the emitted signal power $P_T(R)$ and the spatial pulse response $H(R)$ of the optical channel and the target. Thus, a characteristic relationship between the coupled signal power and distance is derived as

$$P_R(R) = \frac{c\eta A_R}{2} \int_0^{\frac{2R}{c}} P_T(R) H\left(R - \frac{ct}{2}\right) dt \tag{4}$$

where c is the speed of light, A_R represents the aperture area of the sensor's optical receiver, and η represents the optical loss of the receiver. The received signal power $P_R(R)$ of a laser signal, over a single pulse signal cycle and at a distance R, can be defined.

However, this model depicts a continuous process. To ensure high dynamic response, vehicular LiDAR typically discerns only the strongest echo or the last echo of a single laser pulse to determine distance. Therefore, this model has certain limitations. Inspired by the laser emission pulse modeling method in [24], we incorporate the energy formula of the classical Dirac-type laser pulses to define the instantaneous power $P_{T\delta}(R)$ of the emitted laser signal below.

$$P_{T\delta}(t) = E_p \delta(t) \tag{5}$$

where $\delta(t)$ is a unit pulse signal and E_p is the total energy of a single-pulse laser.

Combining this with the emission power spectrum in (3), the energy of a single-pulse laser can be calculated as

$$E_p = P_0 \tau_H \tag{6}$$

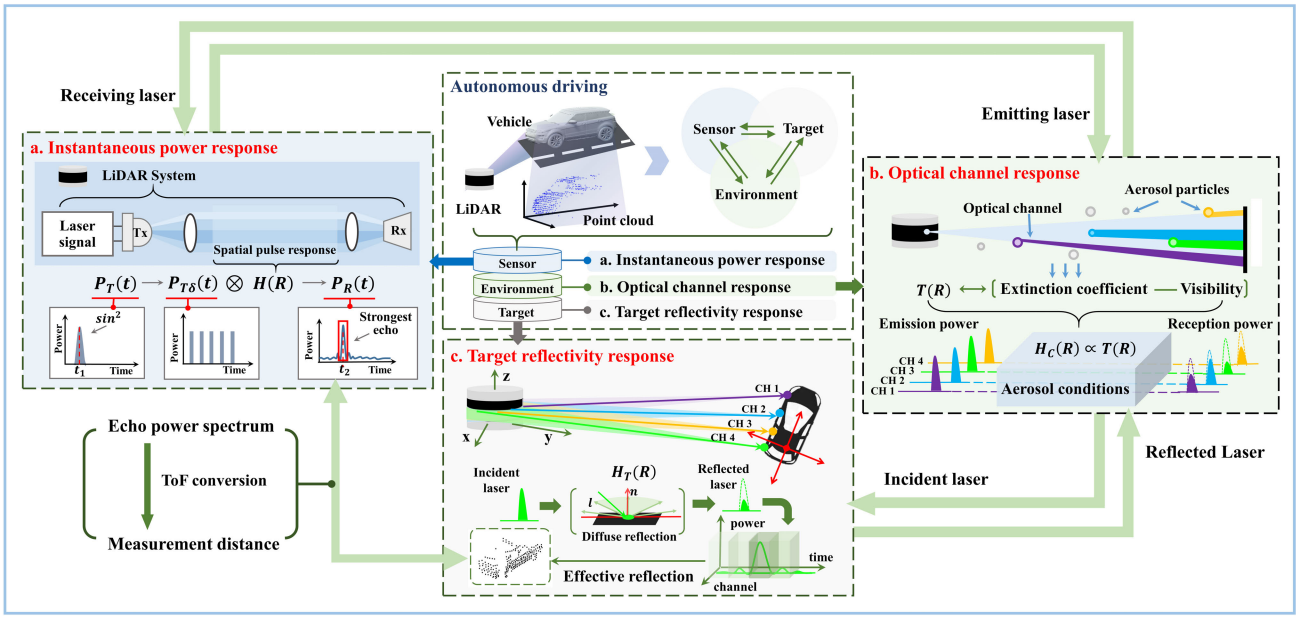

Fig. 3. Coupling modeling of multiple physical responses for LiDAR signals.

Therefore, by combining (4), (5), and (6), and taking the strongest echo power of LiDAR as our analysis target, a complete pulse power model relationship can be defined here.

$$P_R(R) = \frac{c\eta A_R}{2}\int_0^{\frac{2R}{c}} P_0\tau_H\delta(t)H\left(R-\frac{ct}{2}\right)dt = \frac{c\eta A_R}{2}P_0\tau_H H(R). \tag{7}$$

In this context, the spatial pulse response $H(R)$ of the laser stands for the LiDAR's power relationship with environmental targets. This model usually divides into two components: the channel attenuation response $H_C(R)$, reflecting the signal's attenuation in the air, and the target reflection response $H_T(R)$, indicating reflectivity upon laser-target interaction. Thus, $H(R)$ is further detailed as

$$H(R) = H_C(R)H_T(R) \tag{8}$$

2) Optical Channel Response: The channel attenuation response $H_C(R)$ is primarily caused by the concentration of atmospheric aerosol particles. In environmental monitoring, measuring the return power of pulses at different wavelengths can quantify the extinction coefficient γ_{ext} in the air, such as in Raman LiDAR and high-spectral-resolution LiDAR measurements [16]. Based on this principle, we model $H_C(R)$ according to a simplified model of the signal power and aerosol conditions, as

$$H_C(R) = \frac{T^2(R)}{R^2}\xi \tag{9}$$

where ξ denotes the incomplete coverage ratio between the optical emission path and the receiving area.

Given that most vehicular LiDAR employ coaxial emission/reception optics, ξ is typically defined as a distance-independent constant and is designated as 1. Furthermore, $T(R)$ represents the energy attenuation rate related to the laser wavelength. Based on the Beer-Lambert law [35], $T(R)$ is expressed as an exponential function representing the integral of the extinction coefficient γ_{ext} over the optical path distance R, defined as:

$$T_R = \exp\left(-\int_0^R \gamma_{ext}dr\right) \tag{10}$$

where γ_{ext} represents the transmission losses of laser signal attributable to aerosol particles along the optical path. Based on this, $H_C(R)$ can be further deducted as

$$H_C(R) = \exp\left(-2\int_0^R \gamma_{ext}dr\right)/R^2 = \left(\exp\left(-2\gamma_{ext}R\right)\right)/R^2. \tag{11}$$

However, researchers and engineers in the automotive industry prefer readily accessible environmental parameters [36] rather than the characteristics of aerosols. Therefore, we adopt the classic Kim model [37], widely utilized in environmental science, to correlate visibility parameters critical for traffic safety with the γ_{ext}, as follows.

$$\gamma_{ext} = \frac{3.91}{V}\left(\frac{\lambda}{\lambda_0}\right)^{-\alpha} \tag{12}$$

where V represents atmospheric visibility. λ_0 represents the reference wavelength of basis laser, typically set at 550 nm, and λ is the wavelength of the vehicular LiDAR, typically set at 905 nm. α represents the aerosol scale coefficient. According to the distribution of environmental visibility V, α is usually determined using the empirical formula as

$$\alpha = \begin{cases} 0.16V + 0.34 & 1km \le V < 6km; \\ V - 0.5 & 0.5\ km \le V < 1km; \\ 0 & 0.1\ km \le V < 0.5\ km. \end{cases} \tag{13}$$

In subsequent model calculations, when the visibility is less than 0.1km, the corresponding measurement distance will sharply decrease, as shown in Fig. 8 (Section IV). The echoes in the environment may become confused with echoes

from measurement targets, resulting in difficult-to-distinguish measurement noise [38]. This relationship is challenging to comprehensively describe in the non-elastic scattering model of (7). Therefore, we only simulate the visibility range from 0.1 km to 6 km. The extended model for the optical channel attenuation response is given as

$$H_C(R,V) = \begin{cases} R^{-2}\exp\left((1.08)^{-V}\dfrac{-9.27R}{V}\right) & 1\ km \le V < 6km; \\ R^{-2}\exp\left((1.65)^{-V}\dfrac{-10.05R}{V}\right) & 0.5\ km \le V < 1km; \\ R^{-2}\exp\left(\dfrac{-7.82R}{V}\right) & 0.1\ km \le V < 0.5\ km. \end{cases} \tag{14}$$

3) Target Reflection Response: The target reflection response, denoted as $H_T(R)$, primarily describes the power loss due to the reflection of laser after colliding with the target object. In the field of optical imaging, the imaging quality of LiDAR is related to the illuminated surface area S_{AT} and the reflectance ρ_S of the laser on the object surface [39]. The reflective response function $H_T(R)$ of the target object at a distance R_0 from the LiDAR can be defined as

$$H_T(R) = \frac{S_{AT}}{S_T(R_0)}\rho_S\delta(R-R_0). \tag{15}$$

where $S_T(R_0)$ represents the beam cross-section of the laser at R_0. In the virtual environment, R_0 can be determined by the geometric relationship between the objects and sensor.

In traffic scenes, the illuminated surface of the measured target objects (such as vehicles and pedestrians) is equal to the cross-section of the laser beam, i.e., $S_{AT} = S_T(R_0)$. Therefore, the target reflection response $H_T(R)$ on a vehicle LiDAR can be simplified as

$$H_T(R) = \rho_S\delta(R-R_0). \tag{16}$$

Moreover, when laser illuminates the surface of an object, it is reflected in different directions. The reflectivity ρ_S represents the proportion of reflected laser from the target that can be received by the LiDAR receiver. Typically, the reflective surface of traffic objects is presumed to be Lambertian, characterized by predominantly diffuse reflection [40]. The Blinn-Phong diffuse reflection model encapsulates the computation formula for laser reflection as

$$\rho_S = Q_d(\widehat{P}-\widehat{C})\cdot\widehat{N} \tag{17}$$

where Q_d represents the diffuse reflection coefficients, $\hat{P}$ is the normalized position vector of the target object, $\hat{C}$ is the normalized LiDAR position vector, and $\hat{N}$ is the normalized normal vector of the collision point on the surface.

Regarding Q_d, we consider the observation results of the Fresnel term in Physically based Rendering (PBR) in optical rendering [35] and summarize the Q_d of common materials in traffic scenes, as shown in Table I.

TABLE I
THE REFLECTANCE OF COMMON MATERIALS IN TRAFFIC SCENES

Material Types	Reflection Coefficient
Metal	0.57~0.82
Person	0.45~0.75
Glass	0.17~0.22
Wall	0.32~0.44
Road surface	0.16~0.27

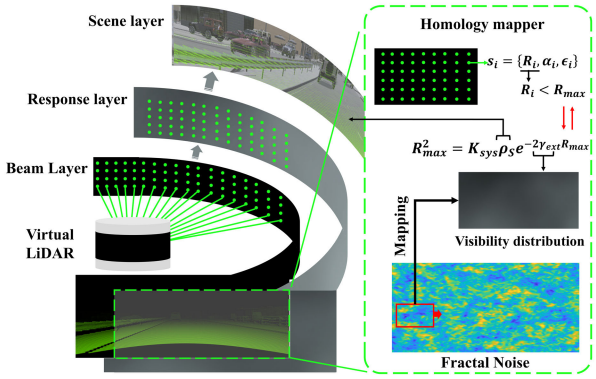

Fig. 4. Schematic diagram of the homology mapping method.

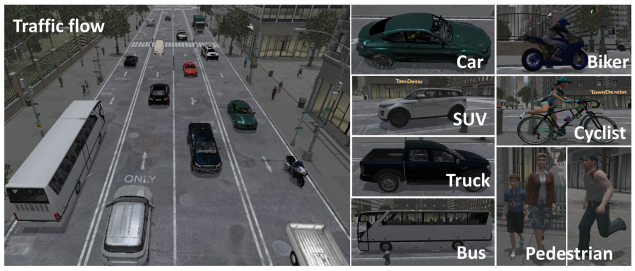

Fig. 5. Virtual traffic scenarios and model details.

C. Coupled Imaging Approach

Based on the previous discussion on a geometric-based LiDAR measurement model, a physical model has incorporated multiple physical components such as power, aerosol attenuation, and reflectance. However, the integration of the measurement model and the physical model remains a challenge. Inspired by the approach of visual shader rendering in computer simulation, we propose a homology mapper for layer-wise modeling of LiDAR perception.

As shown in Fig. 4, we divide LiDAR perception into three layers: 1) the beam layer, which involves the analytical distribution of laser beams based on the measurement model; 2) the response layer, which encompasses the attenuation mapping influenced by environmental parameters on LiDAR measurements; and 3) the scene layer, which represents the three-dimensional reflection relationships formed by the environment, objects, and intersected laser rays.

In computer image rendering, camera simulation overlays pixel points using texture masks [36]. Similarly, based on the spherical coordinate system, we extract the scan points of LiDAR to form an $L \times W$ matrix-like laser emission point array, where L represents the number of point cloud lines and W represents the number of point clouds in the horizontal direction. This can be seen in the top-right part of Fig. 5, where each point corresponds to the geometric relationship

in the measurement model. Therefore, the point array can be further represented below.

$$P_{x,y} = \left\{R_{x,y}, \alpha_{x,y}, \beta_{x,y}\right\}, \ and \ x \in L, \ \ y \in W. \tag{18}$$

Based on the geometric properties of the point array, the response layer is designed to couple the LiDAR measurement model and the physical model. As the physical model involves numerous parameters for calculation, and may lead to unreliable simulations, we construct a concise physical response relationship in the response layer. In a LiDAR system, the effectiveness of laser echo is primarily determined by the receiver's sensitivity threshold, which is defined as P_{min}. That is, when the laser return intensity $P_R(R) \geq P_{min}$, the range measurement signal of the laser can be captured by the LiDAR system. By combining equation (7), the effective spatial response of LiDAR can be expressed as

$$H(R) \geq \frac{2P_{min}}{c\eta A_R P_0 \tau_H}. \tag{19}$$

For a stable LiDAR system, parameters such as P_{min} and A_R are usually constants. Thus, we unify these difficult-to-measure system parameters as

$$H_{sys} = \frac{2P_{min}}{c\eta A_R P_0 \tau_H}. \tag{20}$$

This equation further indicates that the acceptable response threshold is determined by the component performance of the LiDAR. By introducing the light channel attenuation response model and the target reflection response model, the laser reflection power of the target at R_0 can be modeled as

$$H(R) = \frac{\exp(-2\gamma_{ext}R)}{R^2}\rho_S \delta(R - R_0). \tag{21}$$

Assuming that the maximum measurement distance for a single laser beam is R_{max}, we have $P_R(R_{max}) = P_{min}$, which means $H(R)_{max} = H(R_{max})$. Furthermore, by combining equations (19) and (20), we can establish a physical model constraint on the maximum measurement distance in the measurement model. This model is defined as

$$R_{max}^2 = H_{\text{sys}}\rho_S \exp(-2\gamma_{ext}R_{max}) \tag{22}$$

Based on (22), in LiDAR calibration experiments [37], H_{sys} for the LiDAR model can be solved by measuring the maximum distances (R_1, R_2) of two targets with known reflectance $\left(\rho_{s_1}, \rho_{s_2}\right)$. This process is defined as

$$\gamma'_{ext} = \frac{\ln\left(\left(R_1^2\rho_{S_1}\right)/\left(R_2^2\rho_{S_2}\right)\right)}{2(R_2 - R_1)}, \tag{23}$$

$$H_{sys} = \frac{R_1^2}{\rho_1 \exp(-2\gamma'_{ext}R_1)}. \tag{24}$$

where γ'_{ext} denotes the current environmental extinction coefficient. By combining this relationship, we can deduce parameters for different LiDAR types. Table II displays our measurement data for Velodyne and Ouster LiDAR products. Based on this, we further isolate the LiDAR system parameter H_{sys} through the dynamic resolution of (22).

Finally, within the scene layer, we employed computer technology to simulate environmental parameters ρ_S and γ_{ext}, coupling them with the laser physical model. Based on Table I, we assigned the diffuse reflection coefficients for virtual target details related to ρ_S, while utilizing virtual rendering to simulate the environmental visibility distribution associated with γ_{ext}. In this context, fog served as our exemplar for constructing visibility distribution.

TABLE II
CALIBRATION DATA OF DIFFERENT LiDAR PRODUCTS

Product	Velodyne-16	Ouster-128
ρ_{s_1}	0.8	0.8
R_1	120	200
ρ_{s_2}	0.1	0.1
R_2	50	70

Due to the irregular Brownian motion of aerosol particles, the visibility distribution under real conditions is not uniform. There are already many mature applications that can simulate fog visibility distribution in a simulated environment. In this paper, the microscopic motion of aerosols is not our primary focus of research. We employ mature visual fog effect techniques for illustrative simulations. The simulated visibility distribution is mainly based on the fractional Brownian motion rule, which involves the summation of two-dimensional Perlin noise, as shown in the lower-right part of Fig. 5. This simulation method generates a more detailed visibility distribution and can accurately capture the gradient of actual visibility changes.

IV. IMPLEMENTATION AND DEPLOYMENT

A. Experimental Setup

In the experimental design section, our mathematical models developed for LiDAR were primarily validated and applied in a virtual simulation environment. A virtual city-themed autonomous driving scenario was created using the Unity 3D platform. The simulated scene includes urban roads, suburban highways, and park roads, and incorporates highly detailed 3D models of traffic participants such as vehicles, pedestrians, and traffic signs, as shown in Fig. 5.

Subsequently, the algorithm models were executed in script form within the simulation environment. The simulated point clouds were encapsulated in a standard format and output in real-time using UDP transmission. These point clouds can be read and asynchronously encapsulated in ROS to provide perception data for the constructed autonomous driving algorithms. Additionally, the encapsulated point cloud packages can also support offline algorithm testing.

B. Metric Evaluation Methods

To intuitively evaluate the point cloud data generated by our LiDAR model, we conducted similarity assessments between the real point clouds and simulated point clouds of typical objects in the KITTI public dataset [44]. In this regard, the Chamfer distance (CD) and Earth mover's distance (EMD) are two widely used metrics for point cloud similarity evaluation.

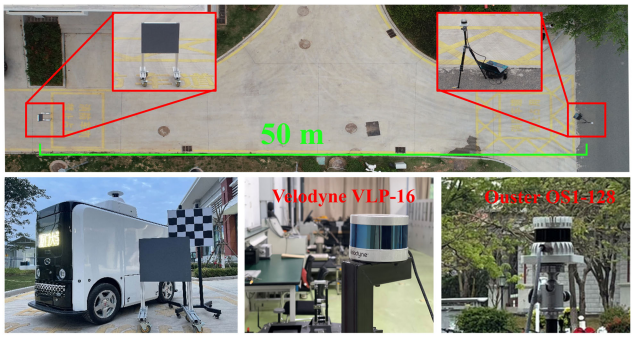

Fig. 6. Experimental equipment and calibration process.

For two registered point cloud sets, C_1 and C_2, their CD is defined as

$$d_{CD} = \frac{1}{|C_1|}\sum_{p\in C_1}\min_{p\in C_2}\|p-q\|_2^2+\frac{1}{|C_2|}\sum_{p\in C_2}\min_{p\in C_1}\|p-q\|_2^2. \tag{25}$$

where p and q are any points in the point sets C_1 and C_2, respectively. On the other hand, EMD is defined as

$$d_{EMD} = \min_{\phi:C_1\to C_2}\sum_{p\in C_1}\|p-\phi(p)\|_2. \tag{26}$$

where $\phi : C_1 \to$ úC_2 represents a one-to-one mapping between the two-point sets. Smaller values of CD and EMD indicate a higher degree of match and greater similarity between the point clouds, further reflecting the suitability of the simulated target point clouds.

C. Hardware and Pre-Trained Model

The experiment employed Velodyne VLP-16 and Ouster OS1-128 LiDAR sensors, installed on King Long autonomous vehicles, as depicted in Fig. 6. The calibration targets for the LiDAR consisted of intensity calibration panels under various reflectance conditions. The experimental scenario was set on the internal roads of Xiamen University's Xiang'an campus.

In the subsequent section of the applicability verification experiments, simulated data can provide input for perception testing in the Kinglong autonomous driving system, where the pre-trained model of the deployed perception algorithm is trained on the publicly available KITTI point cloud dataset. The algorithms compared in this experiment are VoxelNet [45] and PV-RCNN [46], both of which are mature 3D object detection models.

V. Results and Discussion

This section presents a comprehensive analysis on the applicability and effectiveness of the proposed model and its generated point clouds. Section V-A presents a meticulous comparison between the simulated point clouds for various traffic participants and their respective real-world data. Section V-B investigates the fidelity of physical models in capturing LiDAR signal attenuation and imaging nuances within real-world environments, highlighting its applicability in portraying authentic sensing behaviors. Section V-C offers a quantitative analysis of point cloud quality and benchmarks perception algorithm performance using the simulated data. Lastly, additional testing in Section IV-D showcases the model's versatility in broader applications.

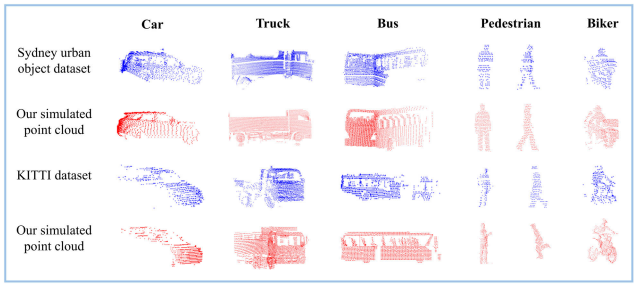

Fig. 7. Point cloud simulation results of LiDAR survey model.

TABLE III
Similarity Evaluation of Simulated Point Clouds at Different Distances

Category		Car	Pedestrian	Biker
0-40m	Truncation	<30 %	<20 %	<20 %
	Size	17.64 m³	0.64 m³	1.78 m³
	Count	>500 p	>140 p	>400 p
	CD	17.12	12.23	15.76
	EMD	14.23	9.45	11.45
40-80m	Truncation	<25%	<15%	<20%
	Size	15.3 m³	0.52 m³	1.61 m³
	Count	100-400p	100-400 p	100-400p
	CD	14.45	10.74	13.86
	EMD	11.26	9.73	10.95
80-120m	Truncation	<15%	<10%	<10%
	Size	13.7 m³	0.46 m³	1.53 m³
	Count	<150p	<100p	<120p
	CD	11.03	9.36	10.56
	EMD	8.55	8.94	8.13

A. Similarity Analysis of Simulated Point Clouds

The similarity and authenticity of simulated point cloud data were compared and validated using public datasets KITTI [46] and Sydney urban objects dataset [47]. By adopting the same measurement angles as those in the reference datasets, we utilized the proposed LiDAR model to produce point cloud data of typical traffic participants within virtual environments. As illustrated in Fig. 7, the morphological attributes and density of our simulated point cloud closely resemble the real-world point cloud data. Furthermore, a quantitative analysis was conducted on the similarity of point clouds across three categories, selected for their equivalence with real data concerning average count, bounding box volume, and occlusion levels. The results are tabulated in Table III.

Overall, the CD and EMD values for the real and simulated point clouds were both recorded below 20, signifying a substantial scale-based similarity between the simulated and actual point clouds. Additionally, we discerned a tendency for the CD and EMD values to decrease as the distance extended. For instance, within the vehicle category ($\Delta_{CD} = 6.09/\Delta_{EMD} = 5.68$), those point clouds pertaining to vehicles situated at farther distances and manifesting lower densities (Count /Volume $<$ 11 p/m^3) conserved the fundamental physical form while attenuating detailed features, a trend that aligns convincingly with the variations observed in real

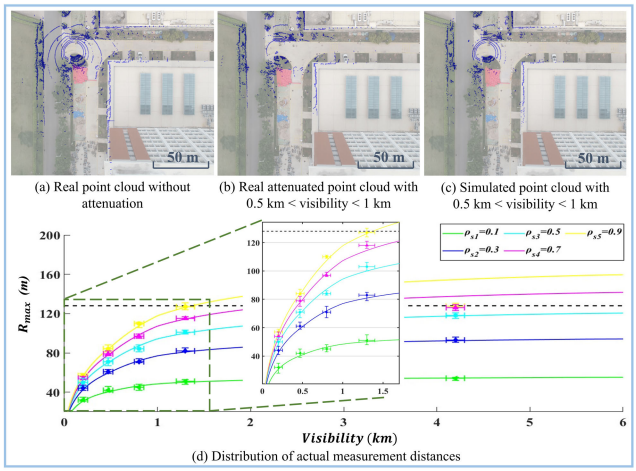

Fig. 8. Comparison of actual attenuation measurement and simulated results.

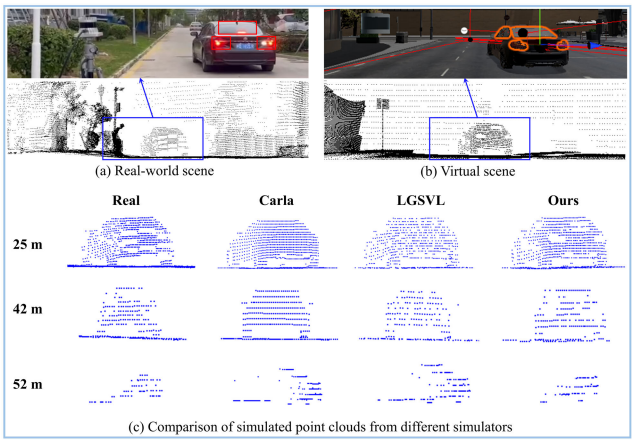

Fig. 9. Simulated point clouds under different distances.

point clouds. These observations indicate that the simulated point clouds exhibit heightened realism at medium to long ranges, a characteristic we attribute to the imaging techniques employed in our introduced physical model.

B. Quantitative Analysis of Physical Properties

To further validate the effectiveness of the proposed LiDAR signal attenuation model, we conducted intensity experiments on calibration boards with different reflectivity in various real-world environments. As shown in Fig. 8, there were three experimental settings: (i) clear weather conditions (visibility $>$ 10 km), (ii) foggy weather (0.5 km $<$ visibility $<$ 1 km), and (iii) slightly hazy conditions (1 km $<$ visibility $<$ 5 km). The calibration boards were diffuse reflectance boards with average reflectivity values of 9.95%, 30.1%, 49.86%, 69.27%, and 89.93%, with a uniformity of +/− 0.27%.

As depicted in Fig. 8(d), under clear weather conditions, the maximum measurement range aligned with the LiDAR's performance parameters, has an average error of +/- 3.03%, which was primarily caused by the LiDAR's scanning process. In foggy and slightly dusty conditions, the measured values were generally distributed along the predicted fitting curve of the attenuation model, with an average error +/- 7.32%. Overall, we believe that this error model exhibits authenticity within a certain range and can be applied for laser attenuation simulation in simulated scenarios.

The authenticity of the physical model employed in the LiDAR framework was further substantiated. Simulations were conducted in a virtual scene replicating the real-world conditions (Visibility $\in [1\ km, 2km]$, glass $Q_d \in [0.17, 0.22]$, metal $Q_d \in [0.57, 0.82]$) concerning the vehicle's position relative to the LiDAR. A comparative analysis was executed between the proposed method and the LiDAR imaging paradigms utilized by Carla and LGSVL. As depicted in Fig. 9, the Carla simulator, restricted to pure geometric modeling, exhibits an excessively comprehensive point cloud. And LGSVL can simulate point cloud sparsity through tailored SNR, but the resulting sparsity deviates significantly from that of actual point clouds. In contrast, the proposed method, by computing environmental variables and material reflectivity, generates a point cloud distribution that is more congruent with reality.

TABLE IV
QUANTITATIVE ASSESSMENT OF SIMILARITY BETWEEN SIMULATED AND REAL-WORLD POINT CLOUDS

Category		Real	Carla	LGSVL	Ours
0-30m	Size	13.41 m^3	14.37 m^3	14.37 m^3	14.37 m^3
	Count	725 p	1174 p	613 p	807 p
	CD	NA	15.45	14.06	12.68
	EMD	NA	13.53	12.88	11.82
	AP_{3D}	82.16%	80.14%	86.31%	85.35%
30-45m	Size	4.61 m^3	7.03 m^3	6.37 m^3	4.87 m^3
	Count	278 p	420 p	253 p	286 p
	CD	NA	14.51	12.07	10.13
	EMD	NA	12.47	10.85	9.38
	AP_{3D}	70.88%	77.49	75.51	71.69
45-60m	Size	2.03 m^3	3.75 m^3	3.66 m^3	2.21 m^3
	Count	103 p	212 p	141 p	121 p
	CD	NA	13.91	13.42	8.14
	EMD	NA	11.15	10.44	7.08
	AP_{3D}	37.06%	63.17%	60.93%	34.13%

To quantitatively analyze the similarity between simulated and real-world point clouds, we assessed average counts and sizes of car point clouds at different ranges. As Table IV indicates, the point clouds from Carla and LGSVL present larger sizes, possibly elevating CD and EMD. In contrast, our simulated point clouds align more closely in both count and size to real data, resulting in smaller CD and EMD. This correlation is further corroborated by the actual 3D object detection results using VoxelNet. Deviant from Carla and LGSVL, which manifest an Average Precision (AP) surpassing 60% at longer distances, our simulated point clouds effectively replicate the genuine fluctuations ($\Delta AP_{3D} = 33.82$) in object detection accuracy within mid-to-long ranges, mirroring the fidelity found in real-world point cloud data.

C. Simulation Test Verification

To validate the effectiveness of the proposed model framework in generating point cloud data, we conducted a quantitative analysis on the generated point cloud data in virtual scenarios. Considering different visibility conditions, we compared the simulated point cloud generated by the measurement model with the point cloud data augmented with environmental parameters. Fig. 10(a) shows the measurement point cloud without signal attenuation, while

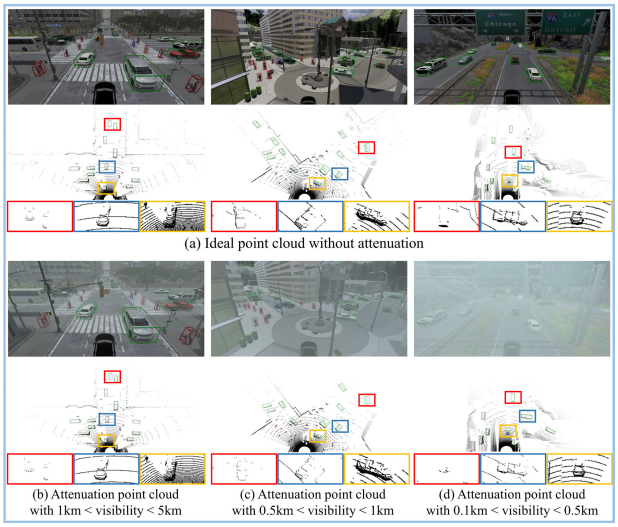

Fig. 10. Simulated point clouds under different visibility.

TABLE V

QUALITY EVALUATION OF SIMULATED POINT CLOUD UNDER DIFFERENT VISIBILITY

Visibility	Distance: 35-70m		Distance: >70m	
	Density	Sparsity	Density	Sparsity
>10 km	21.50 p/m^3	—	10.76 p/m^3	—
1 km ~ 5 km	19.38 p/m^3	9.86%	8.81 p/m^3	18.11%
0.5 km ~ 1 km	18.46 p/m^3	14.14%	8.03 p/m^3	25.29%
0.1 km ~ 0.5 km	17.78 p/m^3	17.30%	7.54 p/m^3	29.87%

TABLE VI

AP_{3D}/AP_{BEV} COMPARISON RESULTS OF DETECTION ALGORITHMS UNDER DIFFERENT ENVIRONMENTAL CONDITIONS

Class	Ideal conditions		1 km < Visibility < 5 km	
	VoxelNet	PV-RCNN	VoxelNet	PV-RCNN
Car	74.42 / 78.56	73.82 / 77.13	71.85 / 76.14	71.57 / 75.39
Pedestrian	60.95 / 64.12	68.22 / 70.99	58.52 / 62.80	66.51 / 69.44
Cyclist	65.06 / 72.49	72.46 / 73.81	63.47 / 70.33	70.90 / 72.62

Fig. 10(b), (c), and (d) depict the attenuated point clouds under different visibility distributions.

It can be observed from Fig. 10(b), (c), and (d) that the point clouds at intermediate distances (35-70m) and far distances (>70m) exhibit varying degrees of sparsity due to changes in visibility, whereas the objects at close distances (<35m) are less affected. To quantify this variation, we performed statistical analysis on the simulated point cloud data, as shown in Table V. Under different visibility conditions, the average density decrease of point clouds at intermediate distances (35-70m) is 9.86%, 14.14%, and 17.30%, while 18.11%, 25.29%, and 29.87% for far distances.

Furthermore, we conducted tests on the simulated point clouds using both VoxelNet and PV-RCNN point cloud detection algorithms, as shown in Fig. 11 and Table VI. Under the no-attenuation condition, both algorithms were able to recognize the traffic objects in the scene, with AP_{3D}/AP_{BEV} slightly lower than the accuracy in the KITTI dataset. This is due to some misidentification phenomena, as shown in Fig. 11 (b) and (c), where the algorithms mistakenly identified buildings and traffic poles as vehicles and pedestrians. Such

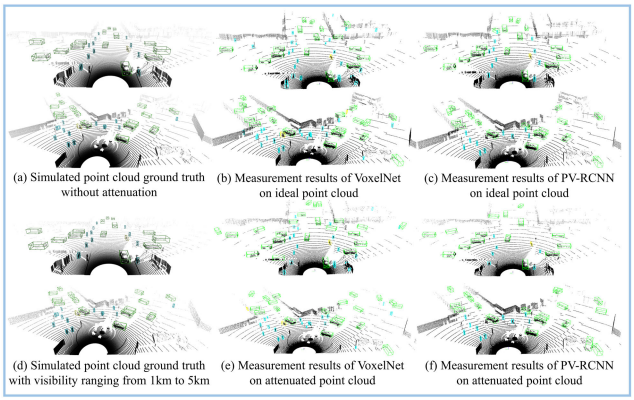

Fig. 11. Comparison results of object detection algorithms.

TABLE VII

AP_{3D}/AP_{BEV} RESULTS OF PV-RCNN UNDER THE CONDITION OF 1~2KM VISIBILITY

Class	AP_{3D}/AP_{BEV} (in %), IoU=0.5		
	<35m	35-70m	>70m
Car	75.65/80.32	74.23/79.83	64.82/66.12
Pedestrian	71.12/74.59	69.75/72.81	58.67/60.93
Cyclist	77.89/79.62	74.23/75.17	60.59/63.08

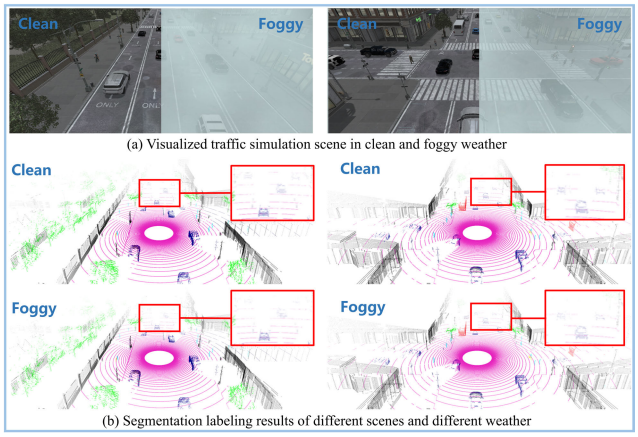

Fig. 12. Point cloud segmentation in foggy environment.

phenomena also exist in real-world scenarios, but the idealized nature of the virtual scene's building models may have slightly exacerbated this issue.

When introducing visibility distributions ranging from 1km to 2km, the detection accuracy of both algorithms generally decreased, as observed in Fig. 11(e) and (f), with more instances of missed detections and false detections of pedestrians and vehicles. This is further supported by the quantitative data in Table VII, which demonstrates that the attenuation of point cloud signals has a greater impact on the detection accuracy of various objects at medium and long distances. Overall, our simulated point clouds are suitable for current algorithm testing, and the attenuated point clouds can evaluate the robustness and applicability of algorithms in challenging environments to a certain extent.

D. Extended Application

Furthermore, the application scenarios for simulated point clouds hold substantial potential for expansion, including

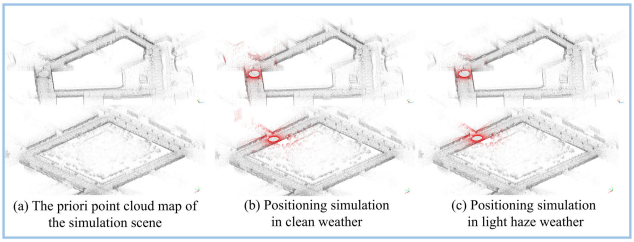

Fig. 13. Autonomous driving positioning test in light haze environment.

point cloud semantic segmentation and map localization in challenging simulated environments. As illustrated in Fig. 12, assigning virtual object category information enables pixel-level semantic segmentation labeling of simulated point clouds. Additionally, as depicted in Fig. 13, high-precision prior point cloud maps can be constructed in virtual environments. By simulating diverse challenging aerosol conditions, we can conduct robustness testing and develop vehicle matching and localization algorithms.

VI. Conclusion

This work presents a hierarchical simulation framework to accurately model the real-world dynamics of LiDAR in autonomous driving scenarios. By hierarchically integrating geometric measurements and physical models within a single framework, the proposed approach successfully solved the challenge of multi-model coupling in LiDAR simulation. Specifically, the homology mapping approach was deployed to correlate the physical variables of the internal LiDAR system and external traffic environment with the geometric model, enabling that the point cloud data remain consistent with dynamic environmental changes during inference generation. Experiments demonstrate that this framework has potential to provide high-fidelity point cloud data for autonomous driving perception across various environments.

As mentioned in Section III, in some extreme environmental conditions such as heavy rain, snowstorms, or dense fog, high-density and large-scale aerosol particles can lead to spurious peaks in the laser signal close to the echo power at incorrect distances, resulting in unpredictable point cloud noise. Therefore, in future work, we will focus on developing richer physical models to better accommodate those extreme environmental conditions. We believe that integrating these environmental conditions will broaden the applicability of the proposed framework.

References

[1] Y. Kang, H. Yin, and C. Berger, "Test your self-driving algorithm: An overview of publicly available driving datasets and virtual testing environments," *IEEE Trans. Intell. Vehicles*, vol. 4, no. 2, pp. 171–185, Jun. 2019.

[2] Z. Liu et al., "Robust target recognition and tracking of self-driving cars with radar and camera information fusion under severe weather conditions," *IEEE Trans. Intell. Transp. Syst.*, vol. 23, no. 7, pp. 6640–6653, Jul. 2022.

[3] D. Feng et al., "Deep multi-modal object detection and semantic segmentation for autonomous driving: Datasets, methods, and challenges," *IEEE Trans. Intell. Transp. Syst.*, vol. 22, no. 3, pp. 1341–1360, Mar. 2021.

[4] A. Knauss, J. Schröder, C. Berger, and H. Eriksson, "Paving the roadway for safety of automated vehicles: An empirical study on testing challenges," in *Proc. IEEE Intell. Vehicles Symp. (IV)*, Jun. 2017, pp. 1873–1880.

[5] L. Li et al., "Artificial intelligence test: A case study of intelligent vehicles," *Artif. Intell. Rev.*, vol. 50, no. 3, pp. 441–465, Oct. 2018.

[6] C. Schwarz and Z. Wang, "The role of digital twins in connected and automated vehicles," *IEEE Intell. Transp. Syst. Mag.*, vol. 14, no. 6, pp. 41–51, Nov. 2022.

[7] Q. Chao et al., "A survey on visual traffic simulation: Models, evaluations, and applications in autonomous driving," *Comput. Graph. Forum*, vol. 39, no. 1, pp. 287–308, Feb. 2020.

[8] Y. Xiao, F. Codevilla, A. Gurram, O. Urfalioglu, and A. M. López, "Multimodal end-to-end autonomous driving," *IEEE Trans. Intell. Transp. Syst.*, vol. 23, no. 1, pp. 537–547, Jan. 2022.

[9] E. Arnold, O. Y. Al-Jarrah, M. Dianati, S. Fallah, D. Oxtoby, and A. Mouzakitis, "A survey on 3D object detection methods for autonomous driving applications," *IEEE Trans. Intell. Transp. Syst.*, vol. 20, no. 10, pp. 3782–3795, Oct. 2019.

[10] J. Fang et al., "Augmented LiDAR simulator for autonomous driving," *IEEE Robot. Autom. Lett.*, vol. 5, no. 2, pp. 1931–1938, Apr. 2020.

[11] A. Dosovitskiy, G. Ros, F. Codevilla, A. Lopez, and V. Koltun, "CARLA: An open urban driving simulator," 2017, *arXiv:1711.03938*.

[12] S. Shah, D. Dey, C. Lovett, and A. Kapoor, "AirSim: High-fidelity visual and physical simulation for autonomous vehicles," 2017, *arXiv:1705.05065v2*.

[13] X. Yue, B. Wu, S. A. Seshia, K. Keutzer, and A. L. Sangiovanni-Vincentelli, "A LiDAR point cloud generator: From a virtual world to autonomous driving," in *Proc. ACM Int. Conf. Multimedia Retr.*, Jun. 2018, pp. 458–464.

[14] Y. Li, P. Duthon, M. Colomb, and J. Ibanez-Guzman, "What happens for a ToF LiDAR in fog?" *IEEE Trans. Intell. Transp. Syst.*, vol. 22, no. 11, pp. 6670–6681, Nov. 2021.

[15] J. P. Richa, J.-E. Deschaud, F. Goulette, and N. Dalmasso, "AdaSplats: Adaptive splatting of point clouds for accurate 3D modeling and real-time high-fidelity LiDAR simulation," *Remote Sens.*, vol. 14, no. 24, p. 6262, Dec. 2022.

[16] R. Marcus, N. Knoop, B. Egger, and M. Stamminger, "A lightweight machine learning pipeline for LiDAR-simulation," in *Proc. 3rd Int. Conf. Deep Learn. Theory Appl.*, Lisbon, Portugal, 2022, pp. 176–183.

[17] T. Shan, J. Wang, F. Chen, P. Szenher, and B. Englot, "Simulation-based LiDAR super-resolution for ground vehicles," *Robot. Auto. Syst.*, vol. 134, Dec. 2020, Art. no. 103647.

[18] F. Taneski, T. A. Abbas, and R. K. Henderson, "Laser power efficiency of partial histogram direct time-of-flight LiDAR sensors," *J. Lightw. Technol.*, vol. 40, no. 17, pp. 5884–5893, Jun. 29, 2022.

[19] C. Goodin, D. Carruth, M. Doude, and C. Hudson, "Predicting the influence of rain on LiDAR in ADAS," *Electronics*, vol. 8, no. 1, p. 89, Jan. 2019.

[20] L. Lin, Y. Liu, Y. Hu, X. Yan, K. Xie, and H. Huang, "Capturing, reconstructing, and simulating: The UrbanScene3D dataset," in *Proc. 31st. Eur. Conf. Comput. Vis. (ECCV)*, vol. 13668, Tel Aviv, Israel, Oct. 2022, pp. 93–109.

[21] J.-E. Deschaud, D. Duque, J. P. Richa, S. Velasco-Forero, B. Marcotegui, and F. Goulette, "Paris-CARLA-3D: A real and synthetic outdoor point cloud dataset for challenging tasks in 3D mapping," *Remote Sens.*, vol. 13, no. 22, p. 4713, Nov. 2021.

[22] D. Kong, X. Li, Y. Cen, Q. Xu, and A. Wang, "Simultaneous viewpoint- and condition-invariant loop closure detection based on LiDAR descriptor for outdoor large-scale environments," *IEEE Trans. Ind. Electron.*, vol. 70, no. 2, pp. 2117–2127, Feb. 2023.

[23] R. Heinzler, P. Schindler, J. Seekircher, W. Ritter, and W. Stork, "Weather influence and classification with automotive LiDAR sensors," in *Proc. IEEE Intell. Vehicles Symp. (IV)*, Jun. 2019, pp. 1527–1534.

[24] R. H. Rasshofer, M. Spies, and H. Spies, "Influences of weather phenomena on automotive laser radar systems," *Adv. Radio Sci.*, vol. 9, pp. 49–60, Jul. 2011.

[25] Y. Wiseman, "Ancillary ultrasonic rangefinder for autonomous vehicles," *Int. J. Secur. Appl.*, vol. 10, no. 5, pp. 49–58, Sep. 2018.

[26] R. Chen et al., "Breaking the temporal and frequency congestion of LiDAR by parallel chaos," *Nature Photon.*, vol. 17, no. 4, pp. 306–314, Apr. 2023.

[27] S. Geiger et al., "Single scattering models for radiative transfer of isotropic and cone-shaped light sources in fog," *Opt. Exp.*, vol. 31, no. 1, p. 125, Jan. 2023.

[28] J. Zhao, Y. Li, B. Zhu, W. Deng, and B. Sun, "Method and applications of LiDAR modeling for virtual testing of intelligent vehicles," *IEEE Trans. Intell. Transp. Syst.*, vol. 22, no. 5, pp. 2990–3000, May 2021.

[29] M. Kutila, P. Pyykönen, M. Jokela, T. Gruber, M. Bijelic, and W. Ritter, "Benchmarking automotive LiDAR performance in Arctic conditions," in *Proc. IEEE 23rd Int. Conf. Intell. Transp. Syst. (ITSC)*, Sep. 2020, pp. 1–8.

[30] T. Yang, Y. Li, Y. Ruichek, and Z. Yan, "Performance modeling a near-infrared ToF LiDAR under fog: A data-driven approach," *IEEE Trans. Intell. Transp. Syst.*, vol. 23, no. 8, pp. 11227–11236, Aug. 2022.

[31] C. Molina et al., "Enhancing sensor capabilities of open-source simulation tools to support autonomous vehicles safety validation," in *Proc. 37th. SAFECOMP*, Västerås, Sweden, 2019, pp. 353–364.

[32] S. Grollius, M. Ligges, J. Ruskowski, and A. Grabmaier, "Concept of an automotive LiDAR target simulator for direct time-of-flight LiDAR," *IEEE Trans. Intell. Vehicles*, vol. 8, no. 1, pp. 825–835, Jan. 2023.

[33] B. Anand, V. Barsaiyan, M. Senapati, and P. Rajalakshmi, "Quantitative comparison of LiDAR point cloud segmentation for autonomous vehicles," in *Proc. IEEE 94th Veh. Technol. Conf. (VTC-Fall)*, Sep. 2021, pp. 1–4.

[34] M. Hahner, C. Sakaridis, D. Dai, and L. Van Gool, "Fog simulation on real LiDAR point clouds for 3D object detection in adverse weather," in *Proc. 18th IEEE/CVF Int. Conf. Comput. Vis. (ICCV)*, Montreal, QC, Canada, Oct. 2021, pp. 15263–15272.

[35] R. Nebuloni, "Empirical relationships between extinction coefficient and visibility in fog," *Appl. Opt.*, vol. 44, no. 18, pp. 3795–3804, Jun. 2005.

[36] P. Testolina, F. Barbato, U. Michieli, M. Giordani, P. Zanuttigh, and M. Zorzi, "SELMA: Semantic large-scale multimodal acquisitions in variable weather, daytime and viewpoints," *IEEE Trans. Intell. Transp. Syst.*, early access, Mar. 28, 2023, doi: 10.1109/TITS.2023.3257086.

[37] I. I. Kim, B. McArthur, and E. J. Korevaar, "Comparison of laser beam propagation at 785 nm and 1550 nm in fog and haze for optical wireless communications," *Proc. SPIE*, vol. 4214, Feb. 2001, pp. 26–37.

[38] M. Bijelic et al., "Seeing through fog without seeing fog: Deep multimodal sensor fusion in unseen adverse weather," 2019, *arXiv:1902.08913*.

[39] A. Asvadi, L. Garrote, C. Premebida, P. Peixoto, and U. J. Nunes, "Real-time deep ConvNet-based vehicle detection using 3D-LiDAR reflection intensity data," in *Proc. 3rd Iberian Robot. Conf.*, Seville, Spain, 2017, pp. 353–364.

[40] F. Wang, H. Shiomi, T. Ito, T. Kakue, and T. Shimobaba, "Fully analytic shading model with specular reflections for polygon-based hologram," *Opt. Lasers Eng.*, vol. 160, Jan. 2023, Art. no. 107235.

[41] A. Tatoglu and K. Pochiraju, "Point cloud segmentation with LiDAR reflection intensity behavior," in *Proc. IEEE Int. Conf. Robot. Autom.*, St. Paul, MA, USA, May 2012, pp. 786–790.

[42] S.-P. Chuah, N.-M. Cheung, and C. Yuen, "Layered coding for mobile cloud gaming using scalable Blinn–Phong lighting," *IEEE Trans. Image Process.*, vol. 25, no. 7, pp. 3112–3125, Jul. 2016.

[43] P. An, Y. Gao, L. Wang, Y. Chen, and J. Ma, "Online extrinsic calibration on LiDAR-camera system with LiDAR intensity attention and structural consistency loss," *Remote Sens.*, vol. 14, no. 11, p. 2525, May 2022.

[44] A. Geiger, P. Lenz, C. Stiller, and R. Urtasun, "Vision meets robotics: The KITTI dataset," *Int. J. Robot. Res.*, vol. 32, no. 11, pp. 1231–1237, Sep. 2013.

[45] Y. Zhou and O. Tuzel, "VoxelNet: End-to-end learning for point cloud based 3D object detection," in *Proc. IEEE/CVF Conf. Comput. Vis. Pattern Recognit.*, Salt Lake City, UT, USA, Jun. 2018, pp. 4490–4499.

[46] S. Shi et al., "PV-RCNN++: Point-Voxel feature set abstraction with local vector representation for 3D object detection," *Int. J. Comput. Vis.*, vol. 131, no. 2, pp. 531–551, Nov. 2022.

[47] M. D. Deuge, A. Quadros, C. Hung, and B. Douillard, "Unsupervised feature learning for classification of outdoor 3D scans," in *Proc. Australas. Conf. Robot. Automat. (ACRA)*, Sydney, NSW, Australia, Dec. 2013, pp. 1–9.

Tengchao Huang (Student Member, IEEE) received the M.Sc. degree in electrical testing technology and instruments from Xiamen University, China, in 2017, where he is currently pursuing the Ph.D. degree in mechanical and electronic engineering. His research interests include the application of virtual simulation technology in intelligent vehicles and autonomous off-road driving systems.

Shuang Song (Student Member, IEEE) received the B.Sc. degree in mechanical engineering from Fujian Agriculture and Forestry University, Fuzhou, China, in 2019. He is currently pursuing the Ph.D. degree with the Department of Mechanical and Electrical Engineering, Xiamen University, Xiamen, China. His research interests include environmental perception and control of autonomous vehicles.

Huosheng Hu (Life Senior Member, IEEE) received the M.Sc. degree in industrial automation from Central South University, Changsha, China, in 1982, and the Ph.D. degree in robotics from the University of Oxford, Oxford, U.K., in 1993. He is currently a Professor with the School of Computer Science and Electronic Engineering, University of Essex, Colchester, U.K. His current research interests include robotics, mechatronics, human–robot interaction, embedded systems, and pervasive computing. He is a Founding Member of the IEEE Robotics and Automation Society Technical Committee on Networked Robots and a fellow of the Institution of Engineering and Technology and the Institute of Measurement and Control, U.K. He is an Executive Editor of *International Journal of Mechatronics and Automation*.

Yunlong Gao received the M.Sc. degree in computer science from Lanzhou University in 2005 and the Ph.D. degree in control science and engineering from Xi'an Jiaotong University in 2011. He is currently an Associate Professor with Xiamen University. His research interests include pattern recognition, machine learning, and data mining.

Guifang Shao received the B.Sc., M.Sc., and Ph.D. degrees in control theory and control engineering from Chongqing University, China, in 2000, 2003, and 2007, respectively. She is currently an Associate Professor with the Pen-Tung Sah Institute of Micro-Nano Science and Technology, Xiamen University. Her research interests include robot control, image processing, and pattern recognition.

Qingyuan Zhu (Senior Member, IEEE) received the Ph.D. degree in vehicle engineering from China Agricultural University in 2009. He was a Visiting Scholar with the University of Illinois at Urbana–Champaign, USA, in 2007, for the joint Ph.D. training, and conducted research at Purdue University, USA, in 2018. He is currently the Dean of the Department of Mechanical and Electronic Engineering, Xiamen University. His research interests include unmanned driving systems and intelligent sensors.